J Mater Sci: Mater Electron **(2024) 35:601**

Effect of gamma rays on magnetic and linear/nonlinear optical properties of pristine and modified nickel ferrite nanoparticles

N. Yousefpour Novini[1], K. Jamshidi-Galeh[2], S. H. Reza Shojaei[1,3,*], T. Tohidi[4], A. Fatemi[2], and Şahın Uyaver[5,6]

[1] *Department of Physics, Faculty of Science, Sahand University of Technology, Tabriz 51335-1996, Iran*
[2] *Department of Physics, Azarbaijan Shahid Madani University, Tabriz, Iran*
[3] *X-LAB, Hasselt University, Agoralaan, 3590 Diepenbeek, Belgium*
[4] *Northwest Research Complex (Bonab), Radiation Application Research School, Nuclear Science and Technology Research Institute, Tehran, Iran*
[5] *Technology Faculty, Marmara University, Maltepe, Istanbul, Turkey*
[6] *Gray Valley Technology Institute, Koycegiz, 48800 Mugla, Turkey*

Received: 6 June 2023
Accepted: 6 March 2024
Published online: 19 March 2024

ABSTRACT

In this study, pure and surfactant-added nickel ferrite nanoparticles are successfully synthesized using the co-precipitation method. The prepared samples are investigated before and after irradiation of gamma ray and compared. The linear and nonlinear optical responses, morphological, magnetic, and structural properties are examined using the photoluminescence, ultraviolet–visible spectroscopy, z-scan technique, field emission scanning electron microscopy (FE-SEM), X-ray diffraction (XRD), vibrating-sample magnetometer (VSM), and Raman spectroscopy analysis. The XRD analyses of the samples showed their crystallinity with no significant change after gamma irradiation. The grain sizes of the irradiated and surfactant-added nickel ferrites are decreased. According to the FE-SEM images, the synthesized particles are spherical. Based on the VSM results, the nanoparticles displayed superparamagnetic properties. However, after gamma irradiation and adding the surfactant, the magnetic saturation is reduced. The band gap of unmodified samples is measured in the range of 2.05–3.92 eV before and after gamma irradiation. Moreover, the band gap of the nickel ferrite samples modified with cetyltrimethylammonium bromide-tartaric acid is in the range of 2.07–3.84 eV. The closed- and open-aperture z-scans are used to measure the nonlinear refractive index and absorption coefficient, respectively. Based on analysis and data, our synthesized nanoparticles can be a good candidate for various applications such as hyperthermia, catalysis, and optical switches.

Address correspondence to E-mail: shojaei@sut.ac.ir

https://doi.org/10.1007/s10854-024-12341-w

1 Introduction

Nowadays, nanocrystalline spinel-type oxides, MFe_2O_4 where M is a divalent metal, have drawn much attention due to their unique magnetic properties. Among them, ferrites are very important because of their broad medical applications such as drug delivery and hyperthermia in the treatment of cancer. Spinel-type oxides characterized by AB_2O_4 as A and B in the oxygen face-centered cubic lattice denote the tetrahedral and octahedral sites, respectively. These structural compounds form inverse spinel and Fe^{3+} ions that occupy site A and the remaining M^{2+} and Fe^{3+} ions site B [1–3]. Among various ferrites, nano-sized nickel ferrites are soft magnetic materials with large expansion coefficient, high electrical resistance, low coercive field, high saturation magnetism, low eddy current losses, and high permeability. Therefore, they can be appropriate for optical and magnetic applications [4–6]. Many studies have shown that nickel ferrite nanoparticles have good biocompatibility and exhibit strong superparamagnetic properties (high saturation, high acceptability, coercivity, and zero residual paramagnetic behavior) [7–9].

Particle size has a profound effect on the magnetic behavior, the coercive field, of materials. By reducing the particle size to a critical diameter, the single-domain particles are formed. In these conditions, the formation of the domain wall is not feasible, energetically [5, 10]. The anisotropy and exchange energies are zero, because the magnetic moments of all single-domain particles are aligned with the anisotropy axis (the magnetic energy is only the dominant energy). The anisotropic energy is dominated by the thermal energy of smaller particles and the magnetism is no longer stable. In other words, superparamagnetic compounds are inherently nonmagnetic, but they can be magnetic in the presence of an external field [11, 12].

It is interesting that unmodified nanoparticles tend to accumulate and this leads to the increase in the size of the particles and it can be prevented by adding a surfactant. In addition, surface modification reduces the ferrite nanoparticles toxicity. This allows them to disperse by selecting a suitable solvent for the reaction system, and finally, a stable colloid is obtained. This is chiefly because enough repulsive interaction is obtained in the reaction system [13, 14].

It is known that magnetic nanoparticles, modified by organic compounds, have fundamental magnetic properties, therefore, they can improve the application of some groups including hydroxyl, carboxyl, and amino groups for usage in the future [13]. It should also be noted that the interaction of radiant energy, including gamma radiation, with matter is a very important problem in theory and experiment. When gamma ray is applied to materials, profound changes may occur in its structure. The changes can be in mechanical strength, optical properties, magnetic behavior, and also other physical and chemical properties.

Primary charged particles and high-energy electromagnetic radiation interact with the electronic shell or atomic nucleus of the material. This can lead to the elastic and inelastic scattering of particles and causes stimulation and ionization of atoms, onset of nuclear reactions, and structural damage leading to the elastic and inelastic scattering of particles [15–17].

Nonlinear optical (NLO) response of materials under irradiations of intense laser light can be a result of second- or third-order polarization [18]. In materials with centrosymmetric structure, the third-order (only, odd-order) polarizations can lead to nonlinear responses. The centrosymmetric material refers to a crystal containing a point as inversion center for the symmetry elements. The materials of high-NLO response can be of very practical importance due to their applications in optical switching, optical limiting devices [19], and in many other photonic devices. An optical limiting is a material with NLO response that protects the user's eyes and sensitive optical elements against the damage of intense laser lights. It is a major challenge for researchers to find a material with very short NLO responses and higher linear transmission. The nonlinear material can also be used to monitor and control the transmission of light through the optical fibers or wires [20]. In recent decades, the emergence of all-optical devices that are using photons instead of electrons for transferring and processing the information has encouraged scientists to overcome the challenges of this field. The nonlinear absorption (NLA) and nonlinear refractive index (NLR) are two main parameters of NLO materials that should be measured, accurately [21]. Optical damage level, limiting threshold, and dynamic range are other important parameters that need to be determined in an all-optical device [22]. In 2020, Kalunge et al. observed that after gamma irradiation, the average crystallite size and drift mobility (μ) of zinc ferrite decrease, while DC electrical resistivity increases [23]. Moreover, in 2022, Hanan Al-Ghamdi investigated the effects of gamma

irradiation on the ferroelectric, optical, and structural characteristics of bismuth (Bi)-doped barium titanate, $BaTiO_3$ (BT), namely $Ba_{0.95}Bi_{0.05}TiO_3$ ceramics, abbreviated as Bi:BT [24]. Gamma-ray irradiation transforms various types of controlled defects, such as point defects in clusters and column defects in the bulk material. To the best of the authors' knowledge, the NLO and magnetic properties of modified or gamma-irradiated nickel ferrite nanoparticles have not been investigated. In this work, the effects of gamma irradiation on the linear/nonlinear optical and magnetic properties of modified and unmodified nickel ferrite nanoparticles with cetyltrimethylammonium bromide (CTAB)-tartaric acid surfactant are studied.

2 Experimental procedure

The grade of all chemicals was analytical (Sigma-Aldrich). These chemicals were not further purified and used as received.

2.1 Synthesis of materials

Nickel ferrite nanoparticles (referred to as NF1) were synthesized using the solutions of nickel nitrate and iron nitrate using an easy and cost-effective technique, the co-precipitation method. First, 10 ml of $Ni(NO_3)_2$ (0.4 mol/L) was added to 10 ml of $Fe(NO_3)_3$ (0.8 mol/L) and the resultant solution was stirred for 2 h at a temperature of 40 °C. Surfactant-added nickel ferrite sample (referred to as NF2) was also synthesized under the same reaction conditions by adding the CTAB-tartaric acid (0.1 mol/L) surfactant at a pH of 11. To purify the synthesized samples, they were centrifuged at 5000 rpm for 10 min and repeated for three times. Then, the products were washed with distilled water and ethanol and allowed to dry in oven at 80 °C for 3 h. To improve the crystalline conditions of the samples, they were annealed for 3.5 h in a muffle furnace at 580 °C. All samples were finally exposed to 40 kGy of gamma irradiation. For photoluminescence analysis and z-scan measurements, 15 mg of each sample was dispersed in 10 ml of ethanol.

2.2 Characterization

The synthesized samples were irradiated by a gamma dose of 40 kGy at room temperature using the Gammacell_220 (Nordion, Canada) from a ^{60}Co source with a 1.5 Gy/s dose rate. Fricke dosimeter was used to calibrate the irradiator. After gamma irradiation, pure nickel ferrite and surfactant-added nickel ferrite samples were labeled as NF3 and NF4, respectively. To characterize the crystal structure of the samples, the X-ray diffractometer (XRD: D8-Advance Bruker) with CuKα radiation (λ = 1.5406 Å) was used. Raman analysis was performed using the Almega Thermo Nicolet dispersive Raman spectrometer at a wavelength of 532 nm and a laser power of 30 mW. A field emission scanning electron microscope (FE-SEM: MIRA3 FEG, Tescan) was employed to study the morphology of prepared nanoparticles. An Fp-6200 spectrofluorometer was used for photoluminescence (PL) measurements.

To measure the nonlinear refractive index and absorption coefficient, we have used the open- and closed-aperture z-scan setups as schematically shown in Fig. 1. The CW He–Ne laser beam (Melles Griot, 632.8 nm, 75 mW) was focused using a 100 mm focal length lens on the sample. The beam waist was measured about 73 μm by using the edge-scan method. We have calculated the applied intensity in Rayleigh range to be about 160 W/cm^2. By moving the sample along the beam (z-direction) by a micrometer, the output power was recorded using San Wa Laser Power Meter Lp1 Mobiken Series. The normalized transmission curves for different sample position around the focal point were plotted for both open and closed scan modes.

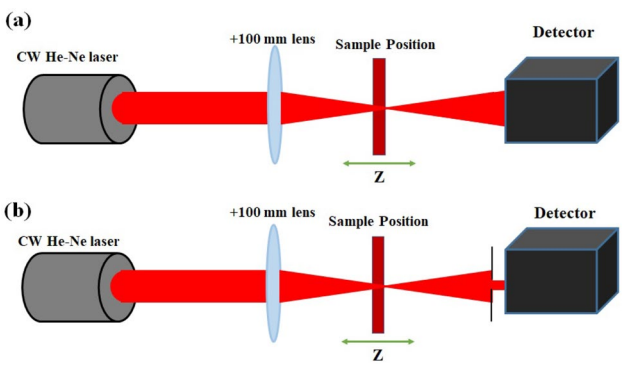

Fig. 1 **a** Open- and **b** closed-aperture z-scan setups for measuring the nonlinear refractive index and nonlinear absorption coefficient

3 Results and discussion

3.1 XRD

$NiFe_2O_4$ has an inverse spinel structure with Ni^{2+} ions at octagonal sites and Fe^{3+} ions evenly distributed between the tetrahedral and octahedral sites [25]. Figure 2 shows XRD spectra of nickel ferrite (black line), nickel ferrite after 40 kGy gamma irradiation (green line), nickel ferrite with CTAB-tartaric acid surfactant (red line), and nickel ferrite with CTAB-tartaric acid surfactant after 40 kGy gamma irradiation (blue line). In the diffraction patterns, the width of the peaks confirms that the samples are nano-sized and the sharp peaks represent highly crystalline structures. According to Fig. 2, the preferred growth at 2θ =35.88° corresponds to the (311) Miller plane of the cubic structure. The characterized peaks appearing at 2θ =30.5°, 37.02°, 43.51°, 54.07°, 57.64°, 63.16°, and 75.01° correspond to (200), (222), (400), (422), (511), (440), and (533) planes of cubic phase nickel ferrite (JCPDS files no. 03-0875), respectively [25].

There are several methods for determining the size of nano-blocks, such as Debye–Scherrer and Halder–Wagner methods. Scherrer's method (Eq. 1) assumes that the Bragg peaks width of X-ray diffraction pattern is due to the size of the nanocrystals and the contribution of other factors, including the imperfections of the crystal lattice, is small compared to this width. Therefore, other factors such as crystal lattice imperfections, which can be caused by lattice displacement, the presence of impurities, lattice dislocations, etc., are not considered. Since these factors cause a strain in the crystal lattice, they affect the width and intensity of the Bragg peaks. From the Halder–Wagner relation (Eq. 2), besides the size of the crystals, the amount of strain in the crystal structure can be obtained as given in the following relation:

$$D = \frac{0.9\lambda}{\beta \cos\theta} \tag{1}$$

$$\left(\frac{\beta^*}{d^*}\right)^2 = \frac{1}{D} \times \left(\frac{\beta^*}{(d^*)^2}\right) + \left(\frac{\varepsilon}{2}\right)^2 \quad \text{where,}$$
$$\beta^* = \frac{\beta \cos\theta}{\lambda},\ d^* = \frac{2\sin\theta}{\lambda}. \tag{2}$$

In Eqs. (1) and (2), D, λ, ε, β, and θ are the size of the nanocrystals, width at half-peak, amount of strain, X-ray wavelength, and diffraction angle, respectively. In Eq. (2), the Halder–Wagner method with the Lorentzian and the Gaussian functions was used to determine the lattice strain (ε) of nickel ferrite nanocrystal. Moreover, d^* denotes the lattice-plane spacing for the reciprocal cell and β^* represents the integral breadth of the reciprocal lattice point. The magnitude of D is directly indicating the nanoparticle strain [26, 27].

According to the Scherrer relation, the particle size is calculated to be 17 nm for NF1, 9.1 nm for NF2, 14.2 nm for NF3, and 8.7 nm for NF4 samples. Also, the Halder–Wagner method is used to estimate the particle size of samples (see Fig. 3). The estimated crystal sizes by two techniques, for all four samples, are summarized in Table 1. In comparison, the data are estimated by two techniques, a difference is seen between the crystal sizes [27]. The large value of D estimated using the Halder–Wagner method may be attributed to large lattice strains [26]. In both cases, after irradiation and addition of surfactant, the particle size is reduced. Even, a 40 kGy dose of gamma ray does not cause a discernible change in the crystallographic phase. As the change in peaks is negligible, the lattice parameters are not changed before and after gamma irradiation.

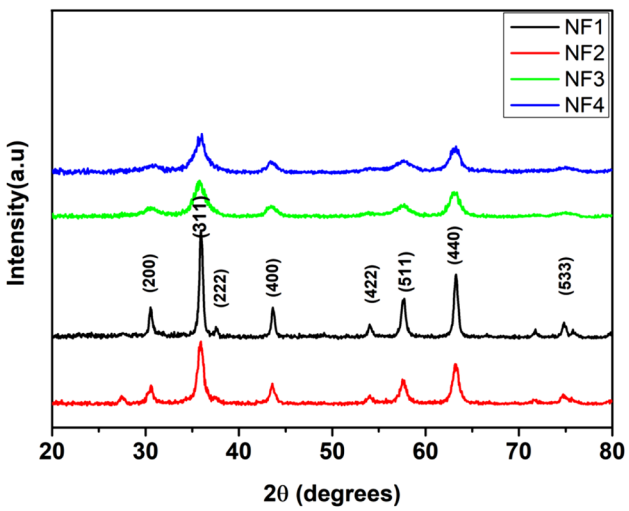

Fig. 2 XRD spectra of NF1, NF2, NF3, and NF4 samples

3.2 Raman studies

The Raman spectroscopy is used to obtain the structural information of the prepared samples. A detailed assignment of all bands observed in the Raman spectra of $NiFe_2O_4$ is not rigorously possible and the assignment might be meaningless since the part of the

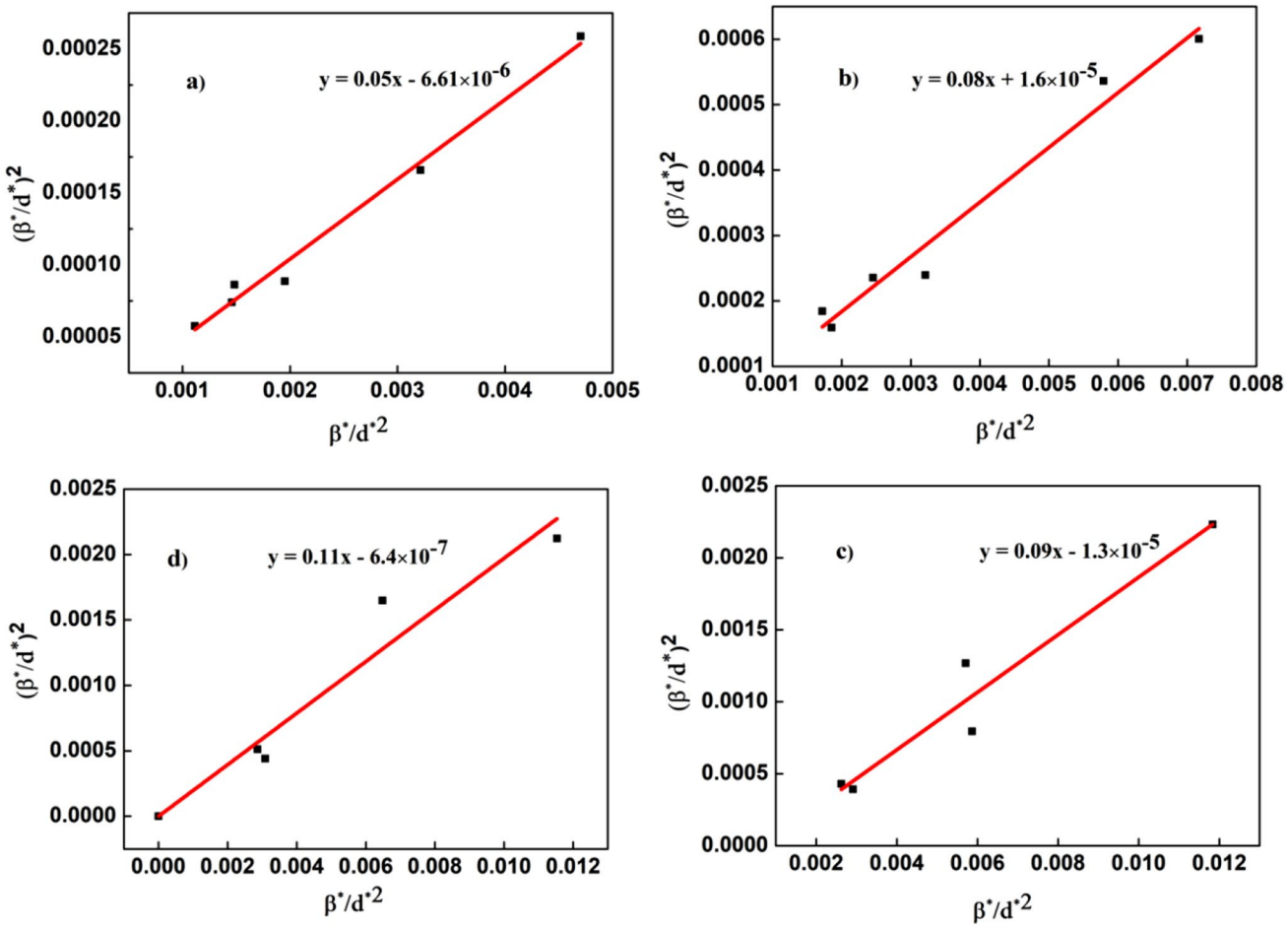

Fig. 3 Particle size distribution of **a** NF1, **b** NF2, **c** NF3, and **d** NF4 samples according to the Halder–Wagner method

Table 1 Strain and crystals size of samples estimated by Scherrer and Halder–Wagner methods

Sample	Halder–Wagner method		Average nanocrystals size by Scherrer method (nm)
	Strain	Nanocrystals size (nm)	
NF1	0.0051	20	17
NF2	0.0040	13	9
NF3	0.0036	11	6
NF4	0.0016	9	8

spectra corresponding to the bands assigned to stretching, bending, rocking, twisting, and wagging modes are very complex [28]. According to the group theory, the inverse spinel ferrites have five main Raman active modes. The standard form of these modes is given by $A_{1g}+E_g+3T_{2g}$ [29]. As it is seen in Fig. 4, the main modes (Raman active peaks) appeared at 153 (T_{2g} (1)), 307

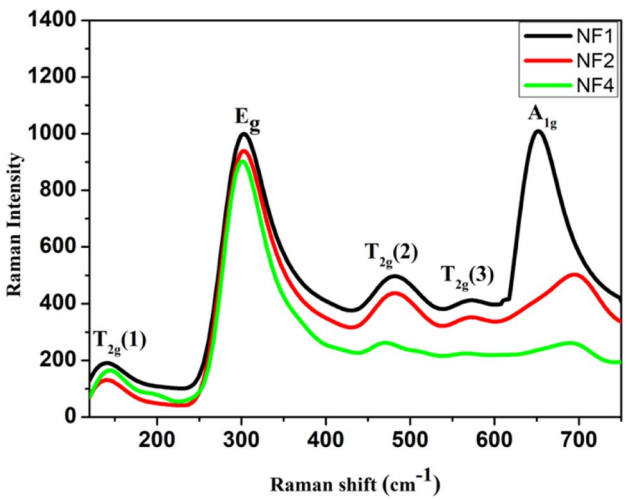

Fig. 4 Raman spectra of NF1, NF2, and NF4 samples

(E_g), 483 (T_{2g} (2)), 572 (T_{2g} (3)), and 692 (A_{1g}). They are measured in unit of cm^{-1} and are in good agreement with the previously obtained results for $NiFe_2O_4$ [30]. The A_{1g} mode occurred by symmetric stretching of oxygen atoms about Fe–O and Ni–O bonds and the E_g mode due to symmetric bending of oxygen atom with reference to the metal ion. Also, the T_{2g} (2) and T_{2g} (3) modes correspond to the vibrations of the octahedral groups. It is believed that T_{2g} (3) results from the asymmetric bending of oxygen and asymmetric stretching of Fe/Ni–O lead to T_{2g} (2). The T_{2g} (1) mode is attributed to the translational movement of the tetrahedron. Moreover, the intensity of the peaks is increased because the grain size increased and therefore the crystallinity of the structure improved. These results are consistent with the XRD results before and after irradiating the samples with gamma ray [29, 30].

3.3 FE-SEM studies

The samples are morphologically analyzed using FE-SEM and the results are presented in Fig. 5. The images confirm the nanoscale structure of the synthesized colloidal particles in all three samples. Moreover, the spherical nanometer particles are uniform and formed an intertwined structure. The uniform structure is very effective in the surface properties of the samples. Micrographs show a change in the grains size and their boundaries. To estimate the nanoparticles size in samples, the surface areas of the formed clusters are measured and calculated by the image processing (ImageJ software). According to the results of adding surfactant (Fig. 5), the particle size is reduced as it was predictable. After gamma irradiation of 40 kGy, the particle size is also reduced. Since γ-photons are able to interact more readily with materials, the photoelectric absorption becomes dominant and reduces the average particle size [31–33].

Figure 6 shows the energy-dispersive X-ray (EDX) spectroscopy of NF1. The inset of this figure shows the atomic and weight percentages of O, Ni, and Fe. The formation of nickel ferrite is confirmed by EDX spectrum and no impurities were observed. So, high-purity samples were prepared.

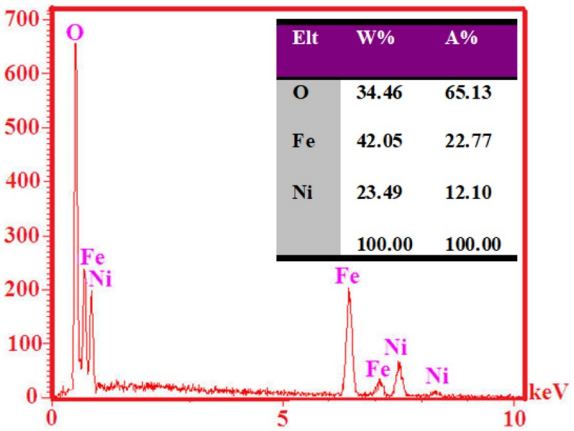

Fig. 6 The EDX analysis of the NF1 sample. Inset table shows the atomic and weight percentages of O, Fe, and Ni

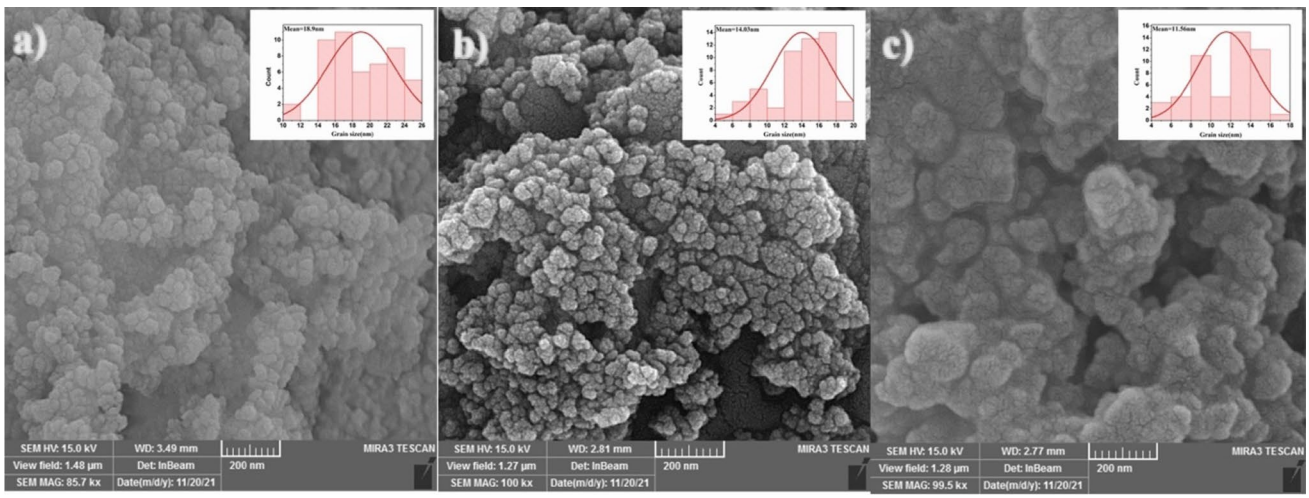

Fig. 5 FE-SEM analysis of **a** NF1, **b** NF2, and **c** NF3 samples

3.4 VSM analysis

In this section, we have presented the VSM results to investigate the magnetic properties (ferromagnetism, superparamagnetism, etc.) of the prepared nanoparticles. For this, the M–H diagram is examined at room temperature by a vibrating magnetometer with applied field ranging from − 15 kOe to +15 kOe. Based on M–H hysteresis, magnetization, and coercive field, the following analysis is done and the properties of the materials are determined. Figure 7 shows the behavior of M–H curve for all samples. It is seen that the hysteresis and coercive field are zero for all samples. This indicates that the nanoparticles are superparamagnetic at room temperature. This phenomenon is often observed when the size of magnetic particles decreases to the critical diameter [26, 34]. Results show that in surfactant-added sample (NF3 in comparison of NF1), the particle size decreases and therefore, the magnetic saturation (M_s) is decreased. It also decreased even more after gamma irradiation (NF2 and NF4 samples) [30, 33–38]. This result indicates that the magnetic properties of nanoparticles can be changed with gamma irradiation. There are some inclined or unordered spins on the surface of the nanoparticles. These spins prevent the alignment of the core spins along the direction of the field so, the M_s of the smaller nanoparticles decreases. This may be attributed to the reduction in magnetic moment interaction and thus a lower magnetization [38]. Moreover, the ions with high energy can penetrate the samples. As a result of inelastic collisions, the gamma photons interact with host atoms and molecules. Depending on the amount of lost energy, this interaction may lead to partial amorphization or defect formation. Therefore, the crystallite size is reduced which in turn causes weakened super-exchange interaction, magnetic dead layers, and spin canting. Furthermore, saturation magnetization is substantially reduced [30, 37, 38].

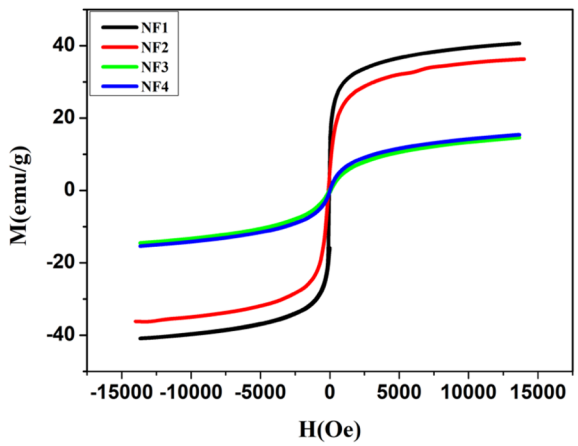

Fig. 7 VSM analysis of NF1, NF2, NF3, and NF4 samples

3.5 Optical properties

3.5.1 UV study

For a solution, the optical absorption coefficient can be calculated using of $\alpha = 2.303\ A\varrho/lc$ [39], where A, ϱ, l, and c are the absorbance, nickel ferrite density (5.368 gcm^{-3}), cell thicknesses (1 cm), and the solution concentration, respectively. According to the Tauc relation, the photon energy is related to the absorption coefficient as $(\alpha h\upsilon)^2 = K\left(h\upsilon - E_g\right)$ [39]. Also, the Kubelka–Munk method can be used to estimate the energy gap. It is expected to get the same results using this method too. As it is based on reflection and partial scattering and as it is known, reflection is related to absorption [40]. In Tauc relation, K is a constant, E_g is the band gap energy, h is the Plank constant, and υ is the frequency of the incident photons. The behavior of $(\alpha h\upsilon)^2$ and $(\alpha h\upsilon)^{1/2}$ versus the photon energy $(h\upsilon)$ is shown in Fig. 8 for all samples. The corresponding optical absorption curve is presented as a inset in each figure. The straight-line parts of the curves can be extrapolated to zero ($\alpha = 0$) to obtain the direct band gap energy E_g. They are estimated for the samples NF1, NF2, NF3, and NF4 as 2.05 eV, 2.07 eV, 3.92 eV, and 3.84 eV, respectively [41, 42]. It is seen that the energy gap of nanostructures, gradually, increases which is a sign of reduced nanoparticle size according to the principle of quantum confinement [43, 44]. These results are in agreement with that obtained from the X-ray diffraction pattern analysis [45]. Likewise, the indirect gap of nanoparticles is also in agreement with the reported results (Fig. 8e) [42].

3.5.2 Extinction coefficient and refractive index

Using the absorption coefficient, the refractive index (n) and extinction coefficient (k) can be calculated. The extinction coefficient is given as the following [40, 46]:

$$k = \frac{\alpha\lambda}{4\pi}, \tag{3}$$

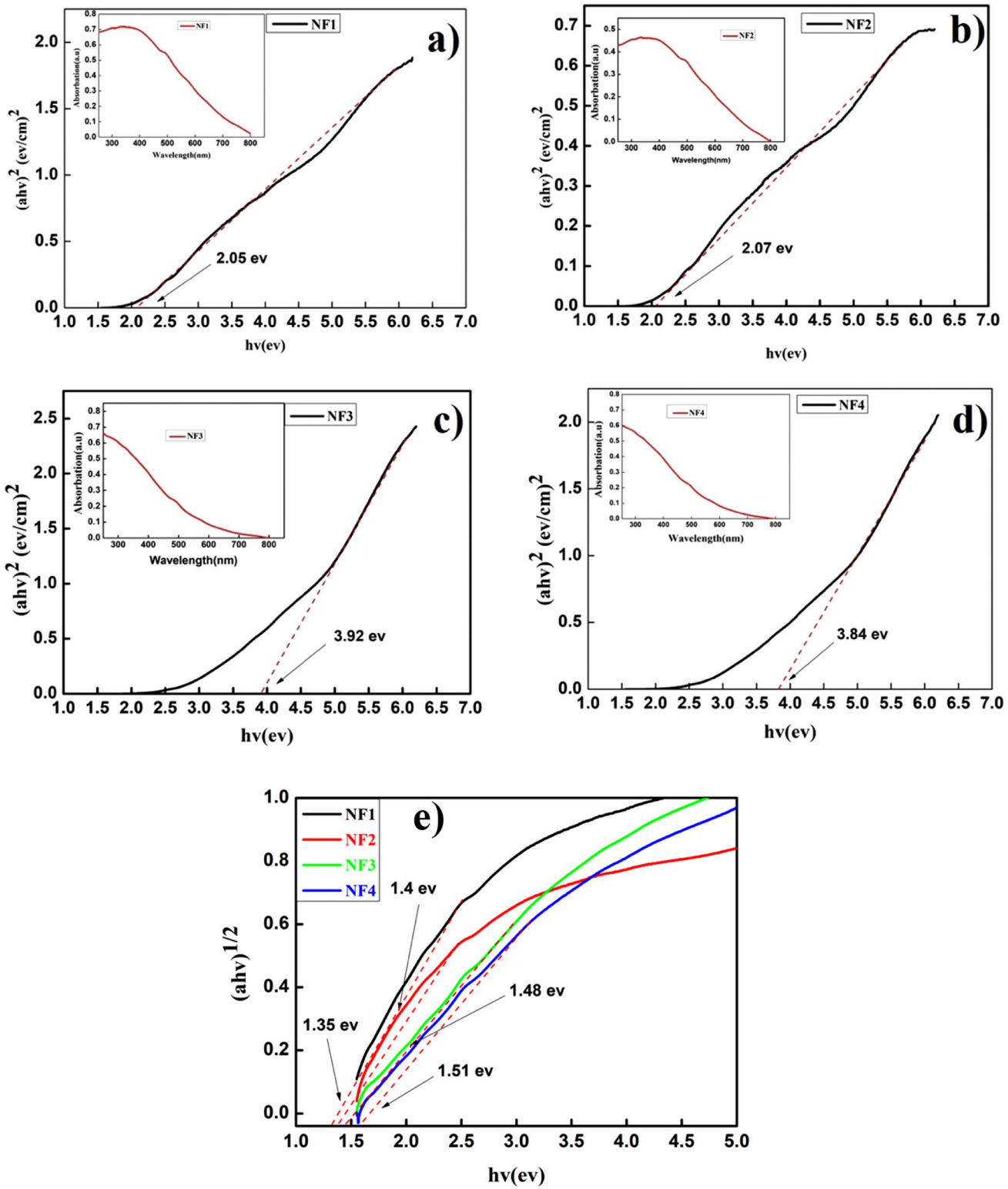

Fig. 8 Variations of $(\alpha h\nu)^2$ against photon energy for direct band gap of **a** NF1, 1 **b** NF2, **c** NF3, **d** NF4 samples, and **e** indirect band gap of samples. The inset of figures shows the absorption of the corresponding samples

where λ denotes the incident photon wavelength. The value of k is a measure of how well a substance can absorb light at a specific wavelength. This value is calculated using the average absorption per unit distance and the fraction of light lost by scattering. On the other hand, in integrated optical applications, the refractive index is one of the basic parameters. The value of the refractive index indicates how a light slows down when it propagates through an optical material [47]. It is related to the local fields inside the material and for the electronic polarizations that can be calculated using the following equation [46]:

$$\left(\frac{1+R}{1-R}\right)+\sqrt{\frac{4R}{(1-R^2)}-k^2}. \tag{4}$$

The behavior of n and k is shown in Figs. 9 and 10 as a function of light wavelength for samples NF1–NF4. There is a direct relation between the extinction and absorption coefficients. It is seen that with increasing the particle size, the absorption and extinction coefficients also increase. The refractive index of all samples decreases with increasing wavelength. Also, it is shifted to lower wavelengths after gamma irradiation. The behavior of optical constants, n and k, in a certain optical spectrum region, is important to identify the materials that are suitable for optical data storage applications [47–49].

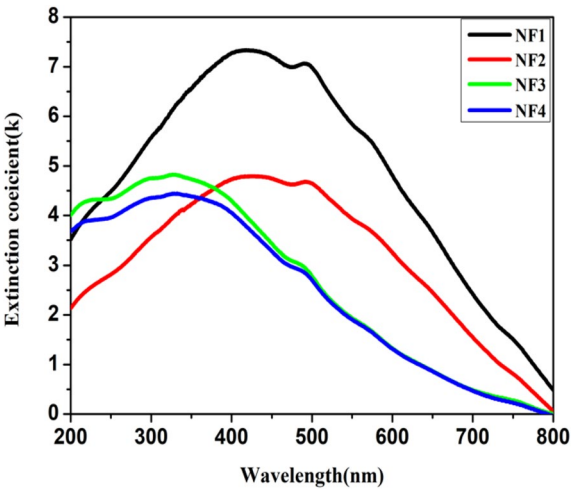

Fig. 9 Behavior of extinction coefficient of NF1, NF2, NF3, and NF4 samples

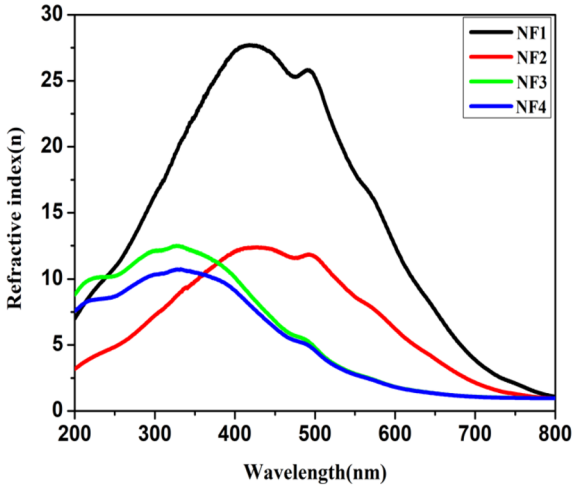

Fig. 10 Refractive index behavior of NF1, NF2, NF3, and NF4 samples

3.5.3 *Nonlinear optical properties*

Figures 11a–d show the open-aperture normalized transmission curves of NF1, NF2, NF3, and NF4 samples, respectively, and their comparison in Fig. 11e. The laser parameters, optical elements, and measurement are explained in section 2.2. The experimental data are then fitted using the following equation to obtain the nonlinear absorption coefficient [50, 51]:

$$T=1-\frac{q_0}{2\sqrt{2}(1+\frac{Z^2}{Z_0{}^2})}, \tag{5}$$

where q_0 is given by $\beta I_0 L_{eff}$, with β and I_0 denoting the nonlinear absorption coefficient and the laser intensity at the beam waist and L_{eff} is the effective length that is given by L_{eff}= (1-exp (α/l))/α with l and α the cell thickness and linear absorption coefficient. In Eq. (5), z_0 is the Riley or diffraction length and relates to beam waist as $z_0=\lambda/\pi w_0{}^2$. The calculated and measured numerical values are summarized in Table 2. The error bars shown on each data are due to errors in reading the numbers on the power meter. Each data is the average of 10 times reading the power meter display. Based on the numerical values of nonlinear absorption coefficient, the saturable absorber behavior is seen with the values of − 24.02, − 4.44, − 6.09, and − 2.67 ($\times 10^{-2}$ cm/W) for NF1, NF2, NF3, and NF4 samples, respectively. It is seen that the saturation decreases and shifts toward the reverse saturation absorption, due to the addition of surfactant and effect of irradiating with gamma rays. Accordingly, it can be obtained

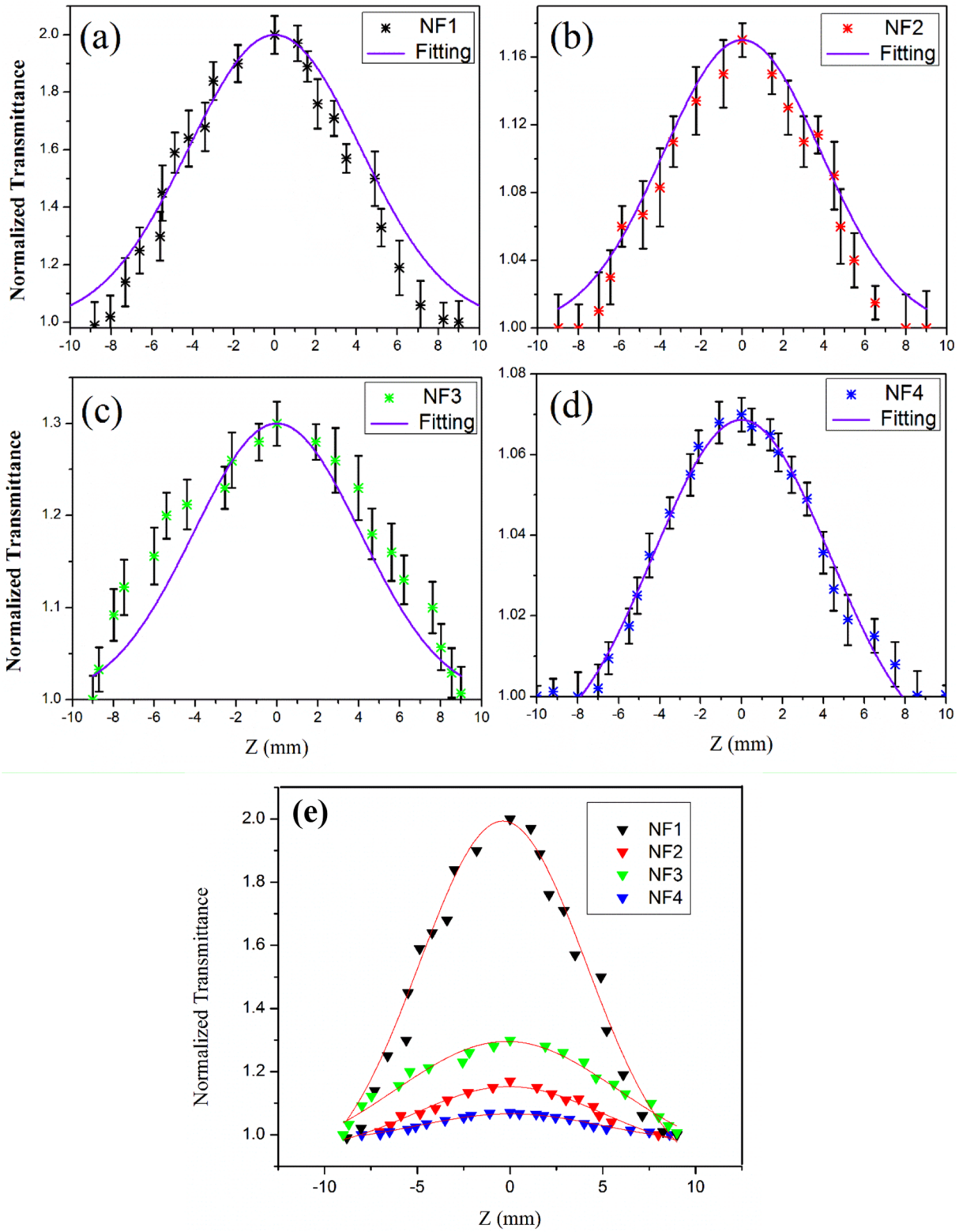

Fig. 11 Nonlinear absorption curves of **a** NF1, **b** NF2, **c** NF3, and **d** NF4. **e** comparison of nonlinear absorption curves of all samples. Error bars show the uncertainty in reading the power meter display. They are the average of ten numbers

Table 2 Numerical values of nonlinear responses, q_0, L_{eff}, and α

Sample	α (1/cm)	$L_{eff} \times 10^{-4}$ (m)	$\Delta\varphi_0$ ($= kn_2I_0L_{eff}$)	q_0 ($= \beta I_0L_{eff}$)	$\beta \times 10^{-2}$ (cm/W)	$n_2 \times 10^{-7}$ (cm^2/W)
NF1	4.91	7.90	0.93	3.03	− 24.02	− 7.41
NF2	7.72	6.96	0.18	0.49	− 4.44	− 1.63
NF3	2.27	8.95	0.46	0.87	− 6.09	− 3.24
NF4	15.94	4.98	0.06	0.21	− 2.67	− 0.83

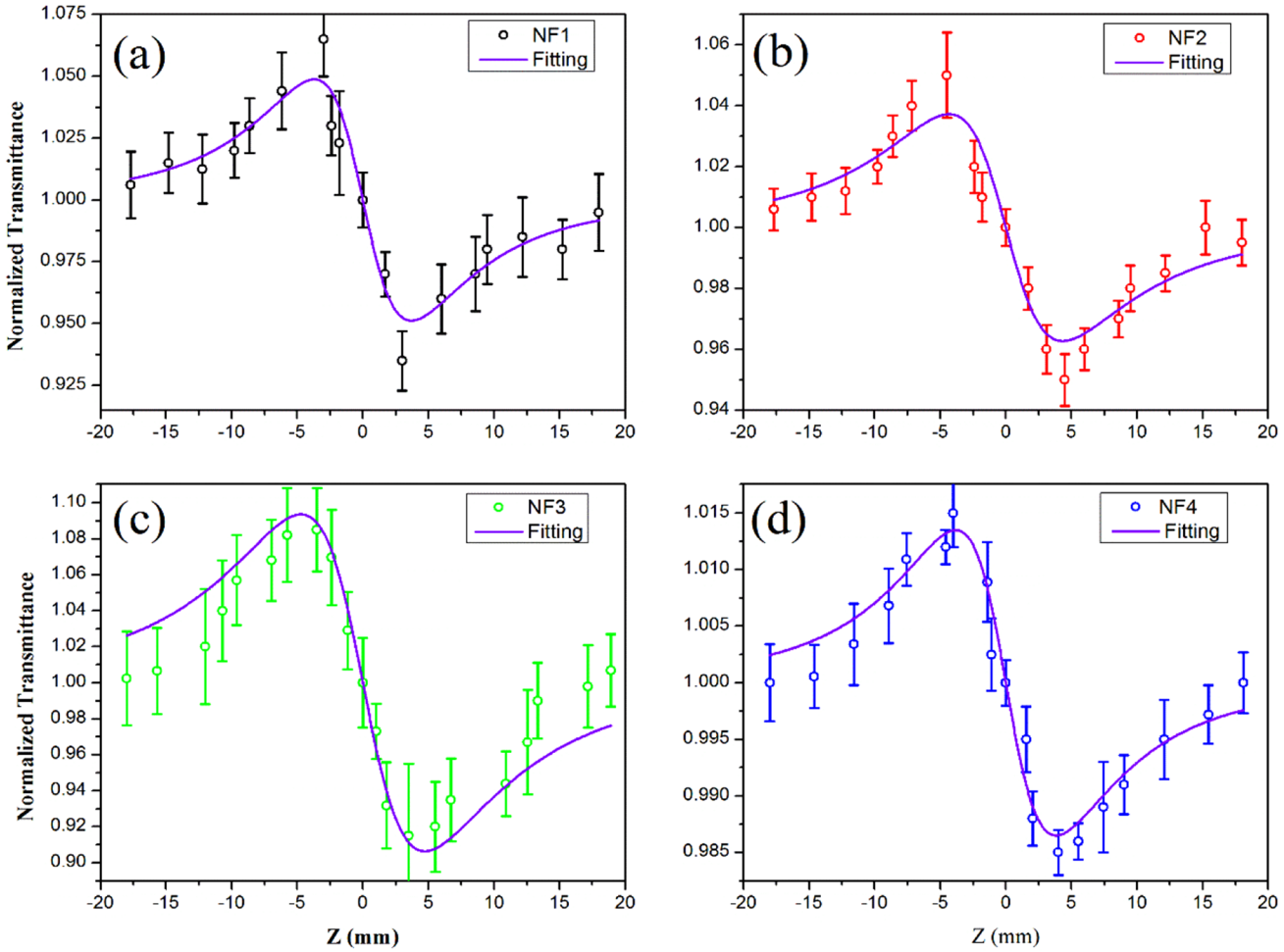

Fig. 12 Closed aperture z-scan experimental curves for NF1 (**a**), NF2 (**b**), NF3 (**c**), and NF4 (**d**) samples. Error bars showing the uncertainty in reading the power meter display and averaged over the ten numbers

that the smaller value of saturation is -2.67×10^{-2} cm/W. Those behaviors predict a good and controllable optical limiting applications.

Figures 12a–d show the normalized closed-aperture z-scan transmission curves for NF1, NF2, NF3, and NF4 samples, respectively. The valley after peak (p–v) behavior of the curves indicates negative sign of the nonlinear refraction corresponding to the self-defocusing phenomena. Same as the nonlinear absorption, it is seen that the nonlinear refraction of gamma-irradiated and surfactant-added samples are also reduced. It is reduced from − 7.41×10^{-7} cm^2/W for the pure $NiFe_2O_4$ to − 3.24×10^{-7} cm^2/W for the gamma-irradiated sample and to − 1.63×10^{-7} cm^2/W

for the surfactant treatment sample. It is further reduced to − 0.83×10^{-7} cm^2/W in the sample treated by both the effects.

The value of nonlinear refractive index can be obtained using the closed-aperture z-scan data by fitting the experimental data with the following equation [52]:

$$T_{p-v} = 1 - \frac{4\Delta\varphi_0 \frac{Z}{Z_0}}{(1+\frac{Z^2}{Z_0^2})(9+\frac{Z^2}{Z_0^2})}. \quad (6)$$

Here, $\Delta\varphi_0$ is defined as $kn_2L_{eff}I_0$, where n_2 is the nonlinear refractive index and k the wavenumber. All the measured parameters are summarized in Table 2. The value of n_2 can be important in a lot of all-optical applications such as optical switching and bistability, optical phases modulation, and conjugation [53, 54].

In comparison, the synthesized $NiFe_2O_4$ sample has been studied under irradiation of CW He–Ne laser with 1600 W/cm^2 applied intensity at different temperatures [9]. The reverse saturable absorption and self-defocusing behavior show that the values of nonlinear absorption and refraction responses decrease with the increase in temperature. In another study, a 532-nm wavelength CW laser has been applied to Zn-doped $NiFe_2O_4$ sample. The reverse saturation absorption and self-defocusing effects have been observed at 100 mW incident laser power [55]. Optical damage is used to describe the vulnerability of materials to high-intensity light and the vulnerability of materials to high-energy laser beams, which can limit applications in devices such as high-intensity optical switches, frequency converters, and amplifiers [56, 57]. It is highly important to produce a type of material with different nonlinear responses such as our synthesized $NiFe_2O_4$ and modified samples. Therefore, surfactant treatment and gamma irradiation can yield to improvement of the nonlinear responses. Figures 11e shows the tunability of the nonlinear responses and this can be very important in various applications.

3.5.4 *Photoluminescence*

Photoluminescence emission occurs as a result of electronic transfer from the higher levels to the lower levels. It is a highly sensitive and nondestructive method for determining the bulk material electronic structure and analyzing the surface defects [27]. In this work,

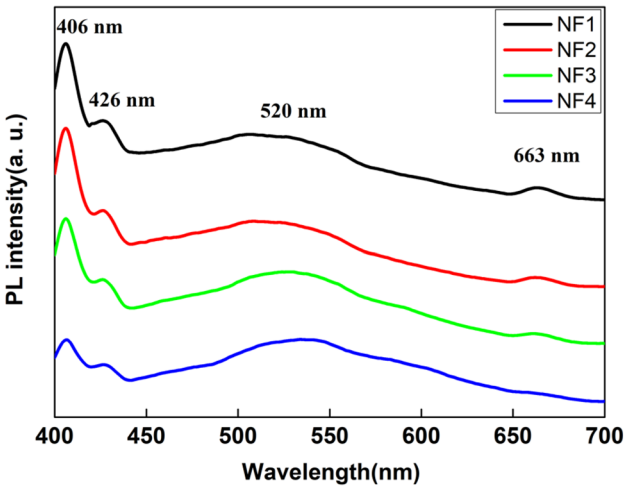

Fig. 13 Photoluminescence spectra of NF1, NF2, NF3, and NF4 samples

the PL of the prepared nanoparticles is measured at room temperature. For this, the excitation wavelength is set to be 380 nm. Figure 13 illustrates the PL spectra of the samples at room temperature in the wavelength ranges of 400–700 nm. Four emission peaks are clearly seen in PL spectra of NF1–NF4. The first one is around 406 nm and results by the electron transitions from the conduction band edge to the trapped holes. The second peak at 426 nm relates to the transitions of Ni^{+2} in octahedral sites. Third peak is around 520 nm, created from $3d^5 \rightarrow 3d^4$ 4s transition of Fe^{+3} ions. The last peak, placed at 668 nm is related to Fe^{3+} in $NiFe_2O_4$, which is located in tetrahedral sites [41, 58]. The intensity of the corresponding peaks varies after gamma irradiation. It is also seen that the intensity of peaks decreases with the decrease in the particle size [49]. The reducing of the intensity decreases the electron–hole recombination. Sharp PL transitions can be useful for applications such as catalyst bases [41, 59].

4 Conclusion

In this work, $NiFe_2O_4$ nanoparticles with Fd3m space group were successfully prepared using the co-precipitation method. The prepared nanoparticles were analyzed using different techniques. They showed superparamagnetic properties at room temperature. We summarized the preparation method, surface modification, and application of $NiFe_2O_4$

nanoparticles. We studied the synthesized particles under irradiation of gamma rays and by adding surfactant. The results showed that the particle size, linear and nonlinear optical properties, and magnetic behavior are modifying. The FE-SEM micrographs showed that particle size distribution is homogeneous without any impurities and it is verified by the EDX spectrum. The X-ray diffraction spectra of samples indicated by their crystallization is a cubic phase with crystal sizes in the ranges of 9–20 nm and 6–17 nm estimated by the Halder–Wagner and Scherrer methods, respectively. Using CTAB-tartaric acid showed a sharp decrease in the particle size in comparison with pure $NiFe_2O_4$ particles. A considerable nonlinear response was measured using the open- and closed-aperture z-scans even at low CW laser intensities. Our analysis showed that the responses can be improved under gamma irradiation and by adding surfactant. This effect introduces them as a good candidate for most important applications in photonics. Finally, the obtained results showed that the proposed treatments make $NiFe_2O_4$ a good candidate for protecting against optical damages.

Acknowledgments

Not applicable

Author contributions

All authors designed the project; N. Yousefpour Novini, T. Tohidi, and K. Jamshidi-Galeh did the experimental design and also carried out measurements; all authors contributed to the writing of the manuscript.

Funding

This project is supported by Sahand University of Technology with contract number 23681.

Data availability

All data generated or analyzed during this study are included in this published article.

Declarations

Competing interests The authors declare no competing interests.

Ethical approval This article does not contain any studies with human participants or animals performed by any of the authors.

Consent to participate The authors declare the consent to participate.

Consent for publication The authors declare the consent for publication

References

1. R.D.K. Misra, S. Gubbala, A. Kale, W.F. Egelhoff Jr., A comparison of the magnetic characteristics of nanocrystalline nickel, zinc, and manganese ferrites synthesized by reverse micelle technique. Mater. Sci. Eng. B **111**, 164–174 (2004)
2. B.E. Kashevsky, V.E. Agabekov, S.B. Kashevsky, K.A. Kekalo, E.Y. Manina, I.V. Prokhorov, V.S. Ulashchik, Study of cobalt ferrite nanosuspensions for low-frequency ferromagnetic hyperthermia. Particuology. **6**, 322–333 (2008)
3. S.P. Gubin, *Magnetic nanoparticles* (Wiley, Weinheim, 2009)
4. V. Sepelak, M. Menzel, I. Bergmann, M. Wiebcke, F. Krumeich, K.D. Becker, Structural and magnetic properties of nanosize mechanosynthesized nickel ferrite. J. Magn. Magn. Mat. **272–276**, 1616–1618 (2004)
5. R. Malik, S. Annapoorni, S. Lamba, V. Raghavendra Reddy, A. Gupta, P. Sharma, A. Inoue, Mössbauer and magnetic studies in nickel ferrite nanoparticles: effect of size distribution. J. Magn. Magn. Mater. **322**, 3742–3747 (2010)
6. T.F. Marinca, I. Chicinas, O. Isnard, V. Pop, F. Popa, Synthesis, structural and magnetic characterization of nanocrystalline nickel ferrite—$NiFe_2O_4$ obtained by reactive milling. J. Alloys Compd. **509**, 7931–7936 (2011)
7. N. Sanvicens, M.P. Marco, Multifunctional nanoparticles properties and prospects for their use in human medicine. Trends Biotechnol. **26**, 425–433 (2008)
8. S. Bhattacharyya, R.A. Kudgus, R. Bhattacharya, P. Mukherjee, Inorganic nanoparticles in cancer therapy. Pharm Res. **28**, 237–259 (2011)

9. H.C. Huang, S. Barua, G. Sharma, S.K. Dey, K. Rege, Inorganic nanoparticles for cancer imaging and therapy. J. Control Release. **155**, 344–357 (2011)
10. A.P. Guimarães, *Principles of nanomagnetism* (Springer, Berlin, 2010)
11. G. Podaru, V. Chikan, in *Magnetism in nanomaterials: applications in catalysis and life sciences*. ed. by S.H. Bossmann, H. Wang (The Royal Society of Chemistry, London, 2017), pp.1–24
12. M. Kalubowilage, K. Janik, S.H. Bossmann, Magnetic nanomaterials for magnetically-aided drug delivery and hyperthermia. Appl. Sci. **9**, 2927 (2019)
13. K. Cheng, S. Hsu, A Facile method to prepare superparamagnetic iron oxide and hydrophobic drug-encapsulated biodegradable polyurethane nanoparticles. Int J Nanomedicine **12**, 1775–1789 (2017)
14. Sh. Liu, B. Yu, S. Wang, Y. Shen, H. Cong, Preparation, surface functionalization and application of Fe_3O_4 magnetic nanoparticles. Adv. Colloid Interface Sci. **281**, 102165 (2020)
15. S. Laurent, D. Forge, M.A. Roch, C. Robic, L.V. Elst, R.N. Muller, Magnetic iron oxide nanoparticles: synthesis, stabilization, vectorization, physicochemical characterizations, and biological applications. Chem. Rev. **108**, 2064–2110 (2008)
16. K.M. Abhirami, R. Sathyamoorthy, K. Asokan, Structural, optical and electrical properties of gamma irradiated SnO thin films. Radiat. Phys. Chem. **91**, 35–39 (2013)
17. A. Manjunath, T. Deepa, N.K. Supreetha, M. Irfan, Studies on AC electrical conductivity and dielectric properties of PVA/NH_4NO_3 solid polymer electrolyte films. Adv. Mater. Phys. Chem. **5**, 295–301 (2015)
18. R.W. Boyd, *Nonlinear optics*, 3rd edn. (Academic press, Cambridge, 2020)
19. A.U. Habeeba, M. Saravanan, T.C.S. Girisun, S. Anandan, Nonlinear optical studies of conjugated organic dyes for optical limiting applications. J. Mole. Struc. **1240**, 130559 (2021)
20. Z. Chai, X. Hu, F. Wang, X. Niu, Ultrafast all-optical switching. Adv. Opt. Mater. **5**(7), 1600665 (2017)
21. J. Wu, Z. Li, J. Luo, A.K.-Y. Jen, High-performance organic second-and third-order nonlinear optical materials for ultrafast information processing. J. Mater. Chem. C. **8**(43), 15009–15026 (2020)
22. J.W. You, S.R. Bongu, Q. Baom, N.C. Panoiu, Nonlinear optical properties and applications of 2D materials: theoretical and experimental aspects. Nanophotonics **8**(1), 63–97 (2019)
23. S. Kalunge, A.V. Humbe, M.V. Khedkar, S.D. More, A.P. Keche, A.A. Pandit, Investigation on synthesis, structural and electrical properties of zinc ferrite on gamma irradiation. J. Phys: Conf. Ser. **1644**(1), 012017 (2020)
24. H. Al-Ghamdi, A.H. Almuqrin, H. Kassim, Effect of gamma irradiation on the structural, optical, electrical, and ferroelectric characterizations of bismuth-modified barium titanate ceramics. Materials **15**(12), 4337 (2022)
25. M. Hjiri, N.H. Alonizan, M.M. Althubayti, S. Alshammari, H. Besbes, M.S. Aida, Preparation and photoluminescence of $NiFe_2O_4$ nanoparticles. J. Mater. Sci: Mater. Elec. **31**, 859–860 (2020)
26. S.K. Abdel-Aal, A.S. Abdel-Rahman, Graphene influence on the structure, magnetic, and optical properties of rare-earth perovskite. J. Nanoparticle Res. **22**(9), 267 (2020)
27. R.M. Chellab, K.H. Harbbi, The correction of the line profiles for x-ray diffraction peaks by using three analysis methods. AIP Conf. Proc. **2123**, 020044 (2019)
28. S.K. Abdel-Aal, A.S. Abdel-Rahman, W.M. Gamal, M. Abdel-Kader, H.S. Ayoub, A.F. El-Sherif, M.F. Kandeel, S. Bozhko, E.E. Yakimov, E.B. Yakimov, Crystal structure, vibrational spectroscopy and optical properties of a one-dimensional organic–inorganic hybrid perovskite of [NH_3CH_2CH (NH_3) CH_2] $BiCl_5$. Acta Crystallogr. B: Struct. Sci. Cryst. Eng. Mater. **75**(5), 880–886 (2019)
29. A. Ahlawat, V.G. Sathe, Raman study of $NiFe_2O_4$ nanoparticles, bulk and films: effect of laser power. J. Raman Spectrosc. **42**(5), 1087–1094 (2011)
30. K.A. Kumar, R.N. Bhowmik, Micro-structural characterization and magnetic study of $Ni_{1.5}Fe_{1.5}O_4$ ferrite synthesized through coprecipitation route at different pH values. Mater. Chem. Phys. **146**(12), 159–169 (2014)
31. Y.S. Rammah, A.S. Abouhaswa, A.H. Salama, R. El-Mallawany, Optical, magnetic characterization, and gamma-ray interactions for borate glasses using XCOM program. J. Theor. Appl. Phys. **13**, 155–164 (2019)
32. O. Agar, H.O. Tekin, M.I. Sayyed, M.E. Korkmaz, O. Culfa, C. Ertugay, Experimental investigation of photon attenuation behaviors for concretes including natural perlite mineral. Res. Phys. **12**, 237–243 (2019)
33. B.P. Rao, K.H. Rao, P.S.V. Subba Rao, A. Mahesh Kumar, Y.L.N. Murthy, K. Asokan, V.V. Siva Kumar, R. Kumar, N.S. Gajbhiye, O.F. Caltun, Swift heavy ions irradiation studies on some ferrite nanoparticles. Nucl. Instruments Methods Phys. Res. Sect. B Beam Interact. Mater. Atoms **244**(1), 27–30 (2006)
34. N.Y. Novini, K. Jamshidi-Galeh, S.R. Shojaei, T. Tohidi, Ş Uyaver, Synthesis and investigation of toxicity and photothermal effect of $NiFe_2O_4$@Cu core-shell nanoparticles. Phys. B: Conden. Matter. **666**, 415114 (2023)
35. A. Karim, S.E. Shirsath, S.J. Shukla, K.M. Jadhav, Gamma irradiation induced damage creation on the cation

distribution, structural and magnetic properties in Ni-Zn ferrite. Nucl. Instruments Methods Phys. Res. Sect. B Beam Interact. Mater. Atoms. **268**, 2706–2711 (2010)
36. R.S. Yadav, I. Kuřitka, J. Vilcakova, J. Havlica, J. Masilko, L. Kalina, J. Tkacz, J. Švec, V. Enev, M. Hajdúchová, Impact of grain size and structural changes on magnetic, dielectric, electrical, impedance and modulus spectroscopic characteristics of $CoFe_2O_4$ nanoparticles synthesized by honey mediated sol-gel combustion method. Adv. Nat. Sci. Nanosci. Nanotechnol. **8**, 045002 (2017)
37. M.S. Hossain, S.M. Hoque, S.I. Liba, S. Choudhury, Effect of synthesis methods and a comparative study of structural and magnetic properties of zinc ferrite. AIP Adv. **7**, 10532 (2017)
38. S.K. Sen, M.M.H. Babu, T.C. Paul, M.S. Hossain, M. Hossain, S. Dutta, M.R. Hasan, M.N. Hossain, M.A. Matin, M.A. Hakim, P. Bala, Gamma irradiated nanostructured $NiFe_2O_4$: effect of γ-photon on morphological, structural, optical and magnetic properties. AIP Adv. **11**, 075308 (2021)
39. E. Filippo, G. Micocci, A. Tepore, T. Siciliano, Fabrication of α-TeO_2 smooth and beaded microwires by thermal evaporation method. J. Cryst. Growth **336**(1), 101–105 (2011)
40. Y.H. Elbashar, A.E. Omran, S.M. Hussien, M.A. Mohamed, R.A. Ibrahem, W.A. Rashidy, A.S. Abdel Rahaman, H.H. Hassan, Molecular and spectroscopic analysis of zinc oxide doped sodium phosphate glass. NLOQO. **52**(3–4), 337–347 (2020)
41. S.W. Xue, X.T. Zu, W.L. Zhou, H.X. Deng, X. Xiang, H. Deng, Effects of post-thermal annealing on the optical constants of ZnO thin film. J. Alloys Compd. **448**, 21–26 (2008)
42. S. Joshi, M. Kumar, S. Chhoker, G. Srivastava, M. Jewariya, V.N. Singh, Structural, magnetic, dielectric and optical properties of nickel ferrite nanoparticles synthesized by co-precipitation method. J. Mol. Struct. **1076**, 55–62 (2014)
43. D. Zhang, X. Pu, K. Du, Y.M. Yu, J.J. Shim, P. Cai, S.I. Kim, H.J. Seo, Combustion synthesis of magnetic Ag/$NiFe_2O_4$ composites with enhanced visible-light photocatalytic properties. Sep. Purif. Technol. **137**, 82–85 (2006)
44. K.M. Garadkar, L.A. Ghule, V.N. Bhoraskar, S.D. Dhole, K.B. Sapnar, (2011) Effects of 6 MeV electron irradiation on ZnO nanoparticles synthesized by microwave method. Proc Part Accel Conf New York 2166–2168.
45. A.R. Chavan, R.R. Chilwar, P.B. Kharat, K.M. Jadhav, Effect of annealing temperature on structural, morphological, optical and magnetic properties of $NiFe_2O_4$ thin films. J. Supercond. Nov. Magn. **31**(9), 2949–2958 (2018)
46. M. Zulqarnain, S.S. Ali, U. Hira, J.F. Feng, M.I. Khan, M. Rizwan, K. Javed, Gh. Farid, M.S. Hasan, Superparamagnetic contributions, optical band gap tuning and dominant interfacial resistive mechanisms in ferrites nanostructures. J. Alloys Compd. **894**, 162431 (2022)
47. Y.H. Elbashar, S.M. Hussien, J.A. Khaliel, D.I. Moubarak, A.S. Abdel-Rahaman, H.H. Hassan, Optical spectroscopic analysis of sodium zinc phosphate glass doped cadmium oxide used for laser window protection. Phys. AUC. **28**, 57–72 (2018)
48. A. Bagade, P. Nagwade, A. Nagawade, S. Thopate, V. Pandit, S. Pund, Impact of Mg^{2+} substitution on structural, magnetic and optical properties of Cu-Cd ferrites. Mater. Today: Proc. **53**, 144–152 (2022)
49. A.H. AL-Hammadi, S.H. Khoreem, Investigations on optical and electrical conductivity of Ba/Ni/Zn/$Fe_{16}O_{27}$ ferrite nanoparticles. Biointerface Res. Appl. Chem. **13**(2), 168 (2023)
50. A. Agrawal, J.Y. Park, P. Sen, G.C. Yi, Unraveling absorptive and refractive optical nonlinearities in CVD grown graphene layers transferred onto a foreign quartz substrate. Appl. Surf. Sci. **505**, 144392 (2020)
51. A. Fatemi, M. Rasouli, M. Ghoranneviss, D. Dorranian, Chemical bath synthesis of Ag_2S, CuS, and CdS nanoparticle-polymer nanocomposites: structural, linear, and nonlinear optical characteristics. Opt. Mater. Ex. **12**(7), 2697–2710 (2022)
52. Z. Dehghani, M. Parishani, M. Nadafan, J.Z. Anvari, Third-order nonlinear optical properties of $NiFe_2O_4$ nanoparticles by Z-scan technique. Optik **144**, 672–678 (2017)
53. S. Yuvaraj, N. Manikandan, G. Vinitha, Effect of Zn^{2+} ions on third order nonlinear optical behavior and power limiting properties of manganese ferrite nanoparticles. Photon. Nanostruc. Fundam. Appl. **45**, 100922 (2021)
54. T.S. Nirmala, N. Iyandurai, S. Yuvaraj, M. Sundararajan, Third order nonlinear optical behavior and optical limiting properties of Ni^{2+} ions doped zinc nano-aluminates. Opt. Mater. **124**, 111950 (2022)
55. P. Surendran, A. Lakshmanan, S.S. Pariya, K. Balakrishnan, Investigations on solid-state parameters of third-order nonlinear optical $Ni_{1-x}Zn_xFe_2O_4$ nanoparticles synthesized by microwave-assisted combustion method. Appl. Phys. A. **126**(4), 257 (2020)
56. Y. Kong, F. Bo, W. Wang, D. Zheng, H. Liu, G. Zhang, R. Romano, J. Xu, Recent progress in lithium niobate: optical damage, defect simulation, and on-chip devices. Adv. Mater. **32**(3), 1806452 (2020)
57. T. Kong, Y. Luo, W. Wang, H. Kong, Z. Fan, H. Liu, Enhanced ultraviolet damage resistance in magnesium

doped lithium niobate crystals through zirconium co-doping. Materials **14**(4), 1017 (2021)
58. BCh. Reddy, H.C. Manjunatha, Y.S. Vidya, K.N. Sridhar, U.M. Pasha, L. Seenappa, C. Mahendrakumar, B. Sadashivamurthy, N. Dhananjaya, B.M. Sankarshan, S. Krishnaveni, K.V. Sathish, P.S.D. Gupta, Synthesis and characterization of multi-functional nickel ferrite nano-particles for X-ray/gamma radiation shielding, display and antimicrobial applications. J. Phys. Chem. Solids **159**, 110260 (2021)
59. R. Saranya, R.A. Raj, M.S. AlSalhi, S. Devanesan, Dependence of catalytic activity of nanocrystalline nickel ferrite on its structural, morphological, optical, and magnetic properties in aerobic oxidation of benzyl alcohol. J. Supercond. Nov. Magn. **31**(4), 1219–1225 (2018)